Physica A 624 (2023) 128927

Contents lists available at ScienceDirect

Physica A

journal homepage: www.elsevier.com/locate/physa

Critical and hysteresis behaviors for a hexagonal core-shell structure nanowire in the Blume–Emery–Griffiths model

G.B. Aziza Goguin [a], T.D. Oke [a,b], R.A.A. Yessoufou [a,b], E. Albayrak [c,*]

[a] Institute of Mathematic and Physical Sciences (IMSP), Dangbo, Benin
[b] University of Abomey-Calavi, Department of Physics, Abomey-Calavi, Benin
[c] Erciyes University, Department of Physics, 38039, Kayseri, Turkey

ARTICLE INFO

Article history:
Received 10 April 2023
Received in revised form 21 May 2023
Available online 26 May 2023

Keywords:
Mean field theory
BEG model
Hysteresis loops
Compensation temperature

ABSTRACT

The magnetic properties and hysteresis loops for the hexagonal Ising nanowire (HIN) with core–shell structure consisting of spin-$\frac{3}{2}$ are considered in the Blume–Emery–Griffiths (BEG) model by using the mean-field approximation (MFA) based on the Gibbs–Bogoliubov inequality for the free energy. The effects of various bilinear and biquadratic interaction parameters between the core, between the shell, and between the core and shell spins are considered for the phase diagrams of the model when temperature $T = 0$ and $T \neq 0$ in addition to the crystal and external magnetic fields effects. The numerical calculations reveal that the model yields first- and second-order phase transition lines and tricritical points. In addition to the isolated critical and critical end-points, the model exhibits at most two compensation temperatures and interesting multiple hysteresis magnetic loops behaviors strongly dependent on the model parameters.

1. Introduction

Nanoparticles are of great technical and research interest because of their interesting magnetic properties in relation to their small size and contact surface [1,2], their capacity to store electrical energy [3,4], their permanent magnetic behaviors [5,6] and ability for high-density information storage [7,8]. Moreover, they have awesome applications in medical field as catalysts, biosensors and drug delivery [9–16]. The nanoparticles are usually considered in the form of nanowires or nanotubes within the core–shell structure and various forms of materials with different spins are used to achieve their desired properties [17].

With the development of nanotechnology, the synthesization of nanoparticles with controllable properties became possible. The Zn–ZnO nanotube complex was synthesized by a solid-vapor process: the ZnO shell has an epitaxial orientation relationship with the Zn crystal core, and the sublimation of Zn leads to the formation of Zn–ZnO nanotubes [18]. Similarly, series of FeNi magnetic nanotubes were fabricated using the pore wetting template method [19]. One-dimensional mesoporous SiO_2 was used as an effective template to obtain the SnO_2 nanotube in controllable form by hydrothermal method and it was shown that the SnO_2 nanotubes, as the anode material in the lithium ion battery, show better performance than the ordinary SnO_2 nanoparticles [20].

Theoretically, several studies on the magnetic properties of nanowires have been carried out using various calculation methods such as: the MFA [21,22], effective-field theory (EFT) with correlations [23–30] and Monte Carlo simulation

* Corresponding author.
E-mail address: albayrak@erciyes.edu.tr (E. Albayrak).

https://doi.org/10.1016/j.physa.2023.128927
0378-4371/

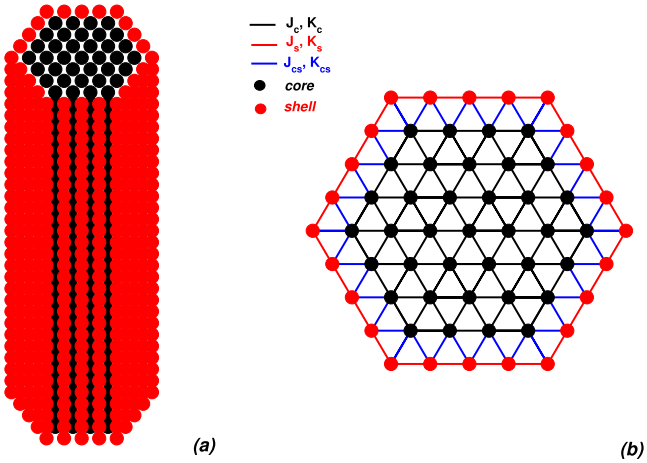

Fig. 1. (a) The schematic representation of Ising nanowire with a hexagonal core–shell structure, (b) The schematic representation of a horizontal layer of hexagonal Ising nanowire.

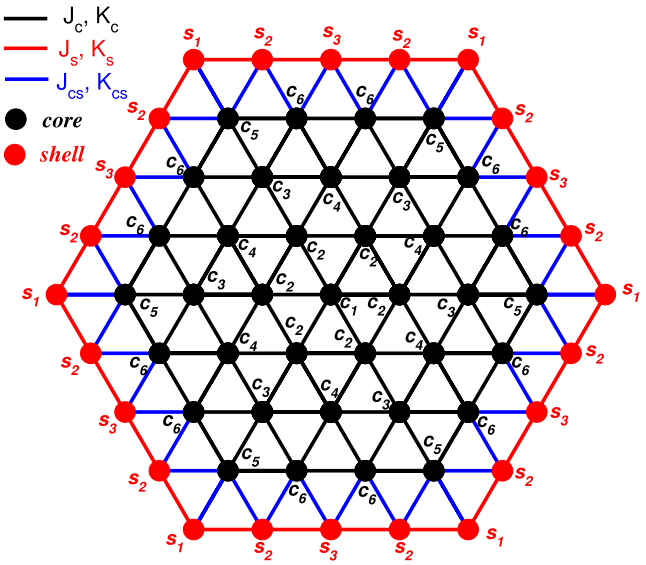

Fig. 2. The schematic representation of sublattices of the nanowire.

(MCS) [31–33]. In addition to these, we can also quote the works as follows: The phase diagrams and the variations of magnetizations was examined in the transverse Ising nanowire with core–shell structure within the EFT [34]. The magnetic properties, compensation temperature, and phase diagrams of ferrimagnetic cylindrical transverse Ising nanotube with a negative core–shell interaction were considered in the EFT [25,35,36]. The crystal field effects were considered for the surface shell of a cylindrical mixed spin-$\frac{1}{2}$ core and spin-1 shell Ising nanotube via the EFT with correlations and, the critical and tricritical points of the model were obtained [37]. The magnetic properties and phase diagrams of a cylindrical spin-1 Ising nanotube were analyzed by using the MCS [38] with the observation of compensation behaviors and triple hysteresis loops. Note that the compensation temperatures appear in ferrimagnetic systems for certain conditions, and have potential applications in thermomagnetic recording and magneto-optical storage media [39,40]. The mixed-spin HIN with core–shell structure was examined by using the MFA based on the Gibbs–Bogoliubov inequality for the free energy [41] and it was shown that the system presents first- and second-order phase transitions, compensation behavior, and critical end points [42]. The magnetic properties and compensation temperatures of a mixed monolayer Coronene-like nanostructure were investigated by using the MCS and interesting magnetic properties of the studied model was revealed [43].

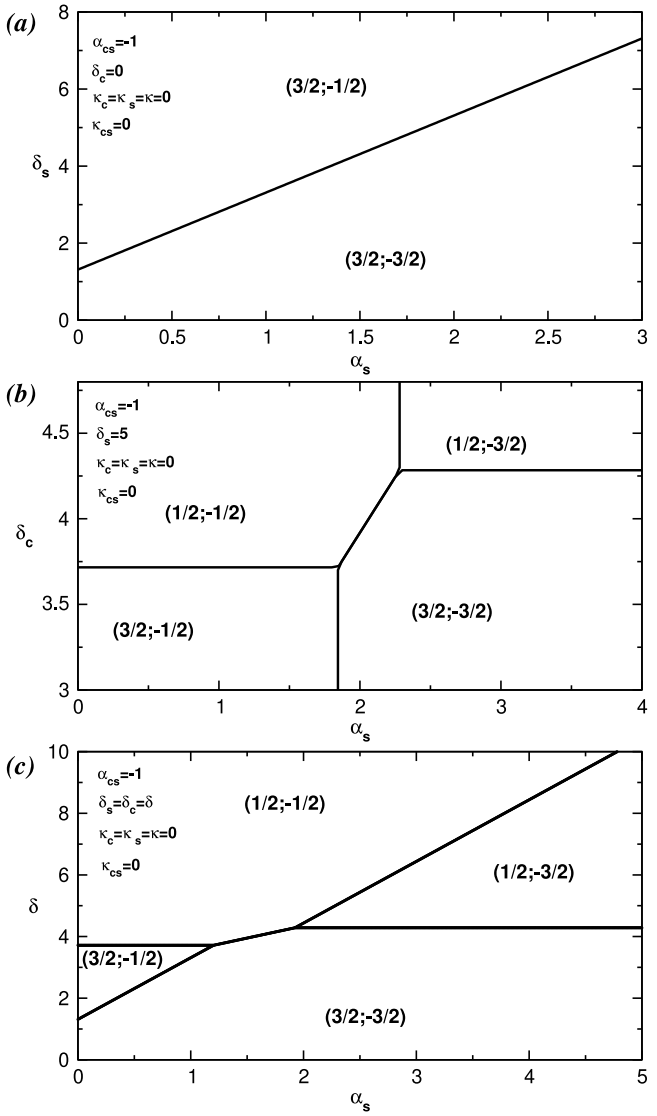

Fig. 3. The ground states phase diagrams; (a) the (α_s, δ_s) plane when $\alpha_{cs} = -1$, $\kappa = 0$, $\kappa_{cs} = 0$ and $\delta_c = 0$), (b) the (α_s, δ_c) plane when $\alpha_{cs} = -1$, $\kappa = 0$, $\kappa_{cs} = 0$ and $\delta_s = 5$) and (c) the (α_s, δ) plane when $\alpha_{cs} = -1$, $\kappa = 0$ and $\kappa_{cs} = 0$.

Additionally, spin-$\frac{3}{2}$ was also considered for the construction nanowires in various forms: The magnetic properties of Blume–Capel model for the HIN with core–shell structure were studied by using the EFT with correlations [44]. Dynamic magnetic properties of the model on a cylindrical nanowire (CIN) in an oscillating magnetic field were investigated within the MFA by utilizing Glauber-type stochastic dynamics [45]. The dynamic phase diagrams depending on the frequency of an oscillating magnetic field and the dynamic hysteresis properties of the kinetic CIN system were studied by means of the mean-field theory based on Glauber-type stochastic dynamics [46]. The magnetization loops of the HIN were examined in the framework of the EFT with correlations based on the differential operator technique [47]. The hysteresis and compensation behaviors of the CIN were considered within the framework of the EFT with correlations and the thermodynamic quantities, such as the total magnetization, hysteresis curves, and compensation behaviors of the system were obtained [48]. It is clear from the above works that the spin-$\frac{3}{2}$ model has not received the well-deserved attention especially for the BEG model which was initially introduced to describe the separation of super fluid phase in the mixed $^3_2$He $-^4_2$ He system [49].

In this work, the magnetic properties and phase diagrams of the HIN consisting of spin-$\frac{3}{2}$ was examined in the BEG model using the MFA with the Gibbs–Bogoliubov inequality for the free energy. The model contains many parameters including the bilinear (J_μ) and biquadratic (K_μ) exchange interaction parameters between the core, shell, and core–shell

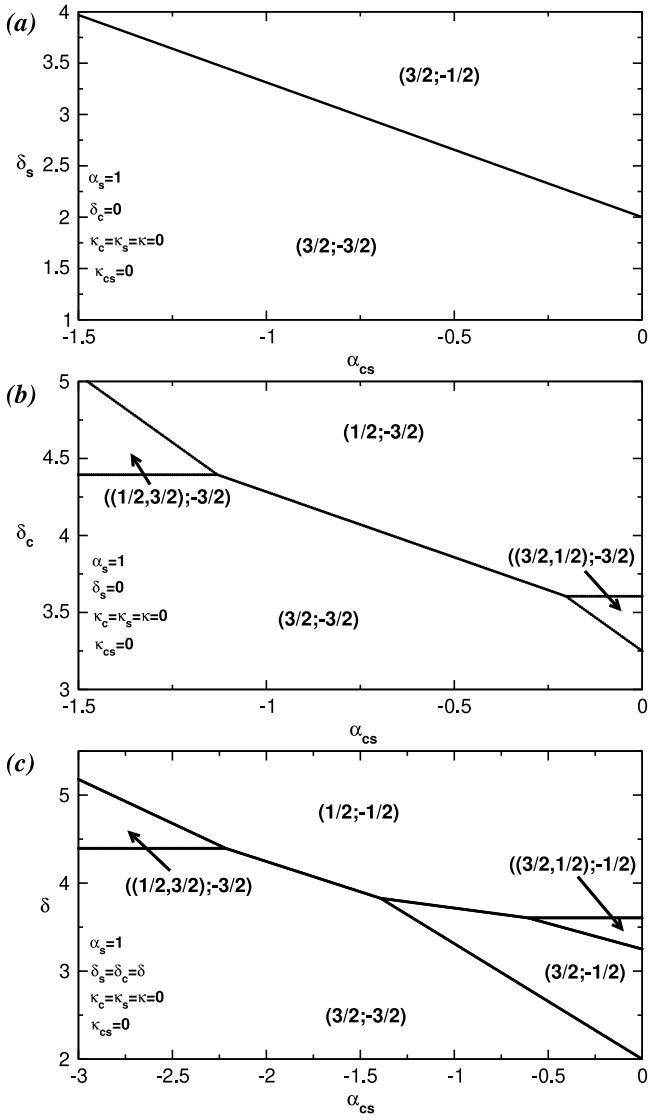

Fig. 4. The ground states phase diagrams; (a) the (α_{cs}, δ_s) plane when $\alpha_s = 1$, $\kappa = 0$, $\kappa_{cs} = 0$ and $\delta_c = 0$, the (b) plane (α_{cs}, δ_c) when $\alpha_s = 1$, $\kappa = 0$, $\kappa_{cs} = 0$ and $\delta_s = 0$ and the (c) (α_{cs}, δ) plane when $\alpha_s = 1$, $\kappa = 0$ and $\kappa_{cs} = 0$.

spins, allowing possible values of crystal field at the core and shell spins (Δ_μ) and equal external magnetic field (h) at all sites. Many aspects of the model, such as the ground state phase diagrams ($T = 0.0$) and the phase diagrams ($T \neq 0.0$) on the possible planes of our system parameters and magnetic hysteresis loops, were considered in great detail.

The remainder of this work is set up as follows: In Section 2, the model and its MFA formalism are presented. In Section 3, we expose and discuss in detail the numerical findings. In final Section, we conclude our investigation.

2. Model and formalism

The studied model is a spin-$\frac{3}{2}$ Ising nanowire with a hexagonal core–shell structure as presented in Fig. 1 where one layer of the HIN consists of $N_c = 37$ sites in the core and $N_s = 24$ sites in the shell giving a total of $N_t = 61$ sites. The nearest-neighbor (NN) core spins interact with the bilinear interaction parameter $J_c = J$ chosen to be greater than zero leading to the ferromagnetic (FM) interactions and with the biquadratic interaction K_c. Similarly, the NN shell spins also interact ferromagnetically with the bilinear interaction parameter $J_s > 0.0$ and with biquadratic interaction coupling K_s. Moreover, there is an antiferromagnetic (AFM) type bilinear interaction coupling $J_{cs} < 0.0$ between the NN core and shell spins in addition to the biquadratic interaction parameter K_{cs}. Each core and shell site of the system are housed in a

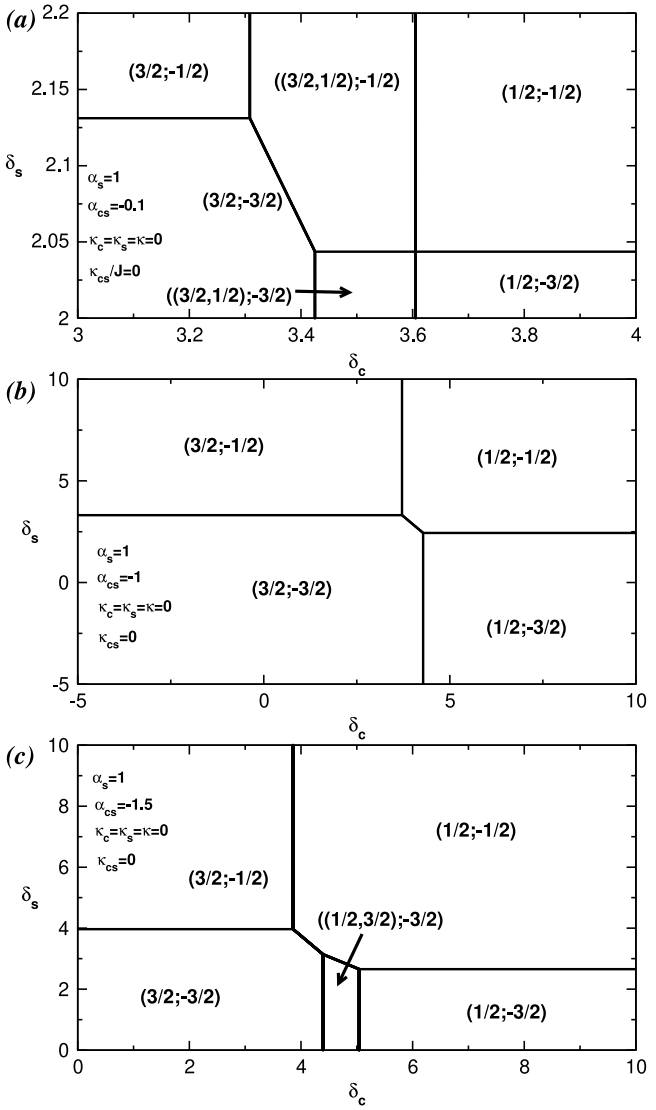

Fig. 5. The ground states phase diagrams for the (δ_c, δ_s) plane when $\alpha_s = 1$, $\kappa = 0$, $\kappa_{cs} = 0$ for (a) $\alpha_{cs} = -0.1$, (b) $\alpha_{cs} = -1$ and (c) $\alpha_{cs} = -1.5$.

uniform crystal field labeled as Δ_c and Δ_s, respectively. A uniform external magnetic field h is also applied to the whole system in order to study the response of the system under magnetic excitation. No need to say that the temperature (T) is the main parameter of the model.

The Hamiltonian of this model including all these internal and external parameters in various forms can be written as follows

$$\begin{aligned}\mathcal{H} = & -J\sum_{\langle i,j\rangle} S_i S_j - J_s \sum_{\langle i,j\rangle} \sigma_i \sigma_j - J_{cs} \sum_{\langle i,j\rangle} S_i \sigma_j - K_c \sum_{\langle i,j\rangle} S_i^2 S_j^2 \\ & - K_s \sum_{\langle i,j\rangle} \sigma_i^2 \sigma_j^2 - K_{cs} \sum_{\langle i,j\rangle} S_i^2 \sigma_j^2 + \Delta_c \sum_i S_i^2 + \Delta_s \sum_j \sigma_j^2 \\ & - h\left(\sum_i S_i + \sum_j \sigma_j\right) \end{aligned} \tag{1}$$

where the core spins are denoted with S_i while the shell spins are indicated with σ_j, and $\langle i, j\rangle$ indicates a summation over the NNs.

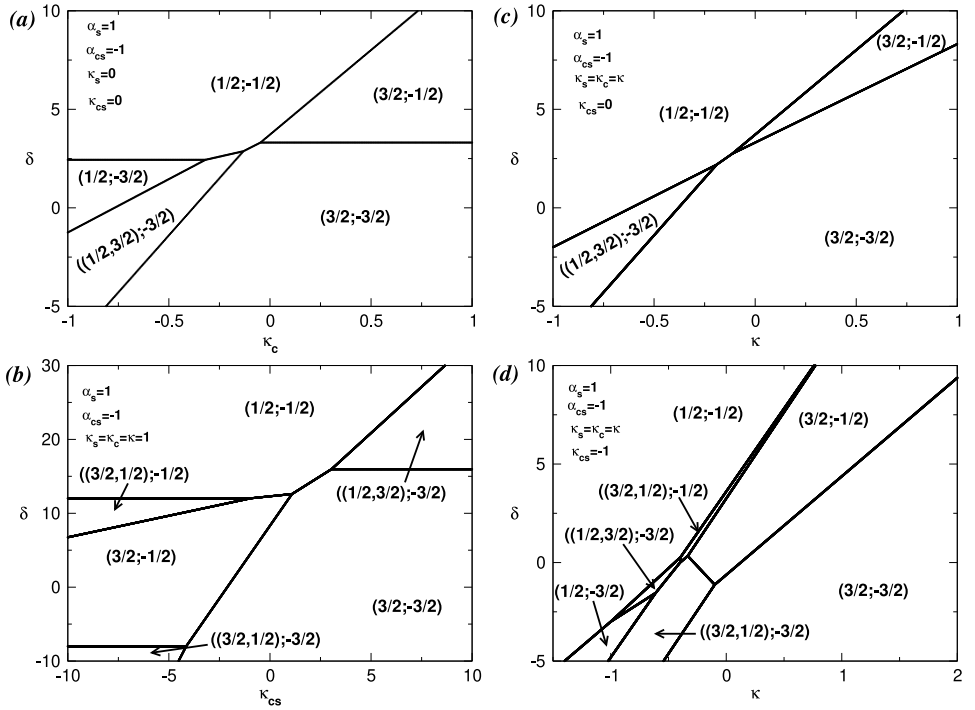

Fig. 6. The ground states phase diagrams; (a) the (κ_c, δ) plane when $\alpha_s = 1$, $\alpha_{cs} = -1$, $\kappa_s = 0$ and $\kappa_{cs} = 0$, (b) the (κ_{cs}, δ) plane when $\alpha_s = 1$, $\alpha_{cs} = -1$ and $\kappa = 1$, (c) the (κ, δ) plane when $\alpha_s = 1$, $\alpha_{cs} = -1$, and $\kappa_{cs} = 0$ and (d) the (κ, δ) plane when $\alpha_s = 1$, $\alpha_{cs} = -1$, and $\kappa_{cs} = -1$.

In order to formulate the model by the MFA, the variational principle based on the Gibbs–Bogoliubov inequality for the free energy [42] was employed by subdividing the system into nine sublattices namely: $(c_1, c_2, c_3, c_4, c_5, c_6)$ for the core section and (s_1, s_2, s_3) for the shell as shown in Fig. 2. Thus, the free energy satisfy the relation given as

$$F \leq F_0(\mathcal{H}_0) + \langle \mathcal{H} - \mathcal{H}_0 \rangle = \phi; \tag{2}$$

where $F(H)$ is the true free energy of the Hamiltonian $\mathcal{H}$ given by the Eq. (1), $F_0(\mathcal{H}_0)$ is the average free energy of an effective Hamiltonian $\mathcal{H}_0$ given as a function of variational parameters and $\langle \mathcal{H} - \mathcal{H}_0 \rangle$ is the average value carried out over the ensemble defined by $\mathcal{H}_0$. The assumed effective Hamiltonian $\mathcal{H}_0$ of the model may have the following form

$$\mathcal{H}_0 = \sum_{j}^{n_j} \sum_{i}^{N} \left(l_j S_i^j + b_j (S_i^j)^2 \right) \quad \texttt{with} \quad j \in \{c_1, c_2, \ldots, c_6; s_1, s_2, s_3\} \tag{3}$$

where N is the number of layers, the values of n_j are given as

$$n_{c1} = 1$$
$$n_{c2} = n_{c3} = n_{c4} = n_{c5} = n_{s1} = n_{s3} = 6$$
$$n_{c6} = n_{s2} = 12$$

and the coefficients are found as

$$\begin{aligned}
l_{c1} &= -J_c(2m_{c1} + 6m_{c2}) - h \\
l_{c2} &= -J_c(m_{c1} + 4m_{c2} + m_{c3} + 2m_{c4}) - h \\
l_{c3} &= -J_c(m_{c2} + 2m_{c3} + 2m_{c4} + m_{c5} + 2m_{c6}) - h \\
l_{c4} &= -J_c(2m_{c2} + 2m_{c3} + 2m_{c4} + 2m_{c6}) - h \\
l_{c5} &= -J_c(m_{c3} + 2m_{c5} + 2m_{c6}) - J_{cs}(m_{s1} + 2m_{s2}) - h \\
l_{c6} &= -J_c(m_{c3} + m_{c4} + m_{c5} + 3m_{c6}) - J_{cs}(m_{s2} + m_{s3}) - h \\
l_{s1} &= -J_s(2m_{s1} + 2m_{s2}) - J_{cs}(m_{c5}) - h \\
l_{s2} &= -J_s(m_{s1} + 2m_{s2} + m_{s3}) - J_{cs}(m_{c5} + m_{c6}) - h
\end{aligned}$$

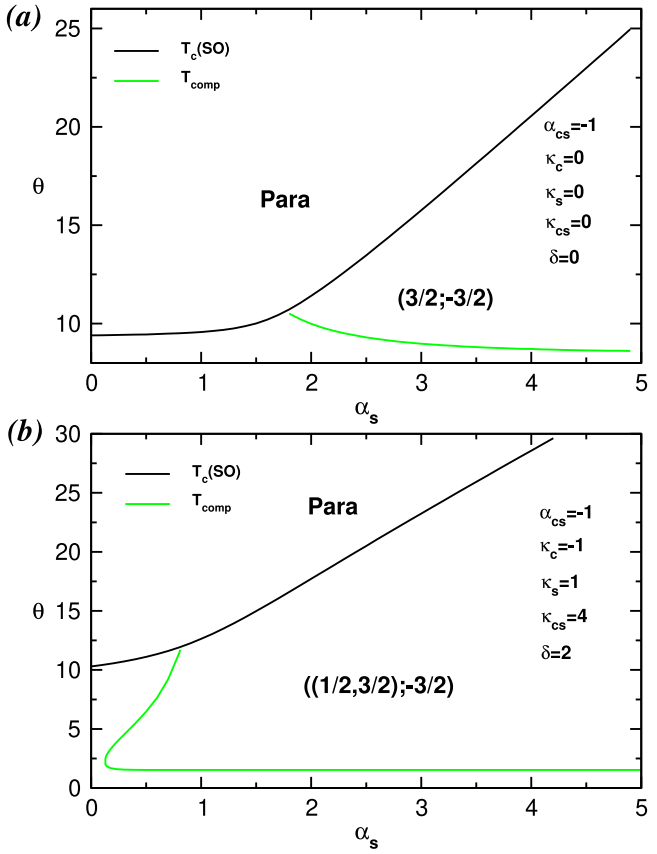

Fig. 7. The dependency of both transition and compensation temperatures on the intralayer exchange α_s when (a) $\alpha_{cs} = -1$, $\kappa = 0$, $\kappa_{cs} = 0$ and $\delta = 0$ and (b) $\alpha_{cs} = -1$, $\kappa_s = 1$, $\kappa_c = -1$, $\kappa_{cs} = 4$ and $\delta = 2$.

$$
\begin{aligned}
l_{s3} &= -J_s(2m_{s2} + 2m_{s3}) - J_{cs}(2m_{c6}) - h \\
b_{c1} &= -K_c(2q_{c1} + 6q_{c2}) + \Delta_c \\
b_{c2} &= -K_c(q_{c1} + 4q_{c2} + q_{c3} + 2q_{c4}) + \Delta_c \\
b_{c3} &= -K_c(q_{c2} + 2q_{c3} + 2q_{c4} + q_{c5} + 2q_{c6}) + \Delta_c \\
b_{c4} &= -K_c(2q_{c2} + 2q_{c3} + 2q_{c4} + 2q_{c6}) + \Delta_c \\
b_{c5} &= -K_c(q_{c3} + 2q_{c5} + 2q_{c6}) - K_{cs}(q_{s1} + 2q_{s2}) + \Delta_c \\
b_{c6} &= -K_c(q_{c3} + q_{c4} + q_{c5} + 3q_{c6}) - K_{cs}(q_{s2} + q_{s3}) + \Delta_c \\
b_{s1} &= -K_s(2q_{s1} + 2q_{s2}) - K_{cs}(q_{c5}) + \Delta_s \\
b_{s2} &= -K_s(q_{s1} + 2q_{s2} + q_{s3}) - K_{cs}(q_{c5} + q_{c6}) + \Delta_s \\
b_{s3} &= -K_s(2q_{s2} + 2q_{s3}) - K_{cs}(2q_{c6}) + \Delta_s.
\end{aligned}
$$

The expression of the approximated free energy per layer $\frac{\phi}{N}$ may be presented as

$$\frac{\phi}{N} = -\frac{1}{\beta}\sum_j n_j \ln \mathcal{Z}_j - \frac{1}{2}\sum_j n_j \left(l_j m_j + b_j q_j\right) + \frac{1}{2}\sum_j n_j \left(-h_j m_j + \Delta_j q_j\right) \tag{4}$$

where $\mathcal{Z}_j = 2\cosh(\frac{3}{2}\beta l_j)e^{-\frac{9}{4}\beta b_j} + 2\cosh(\frac{1}{2}\beta l_j)e^{-\frac{1}{4}\beta b_j}$. By minimizing the free energy with respect to the variational and order parameters, the following mean-field equations are calculated as

$$m_j = -\frac{1}{\mathcal{Z}_j}\left(\sinh(\frac{1}{2}\beta l_j)e^{-\frac{1}{4}\beta b_j} + 3\sinh(\frac{3}{2}\beta l_j)e^{-\frac{9}{4}\beta b_j}\right) \tag{5}$$

$$q_j = \frac{1}{2\mathcal{Z}_j}\left(\cosh(\frac{1}{2}\beta l_j)e^{-\frac{1}{4}\beta b_j} + 9\cosh(\frac{3}{2}\beta l_j)e^{-\frac{9}{4}\beta b_j}\right) \tag{6}$$

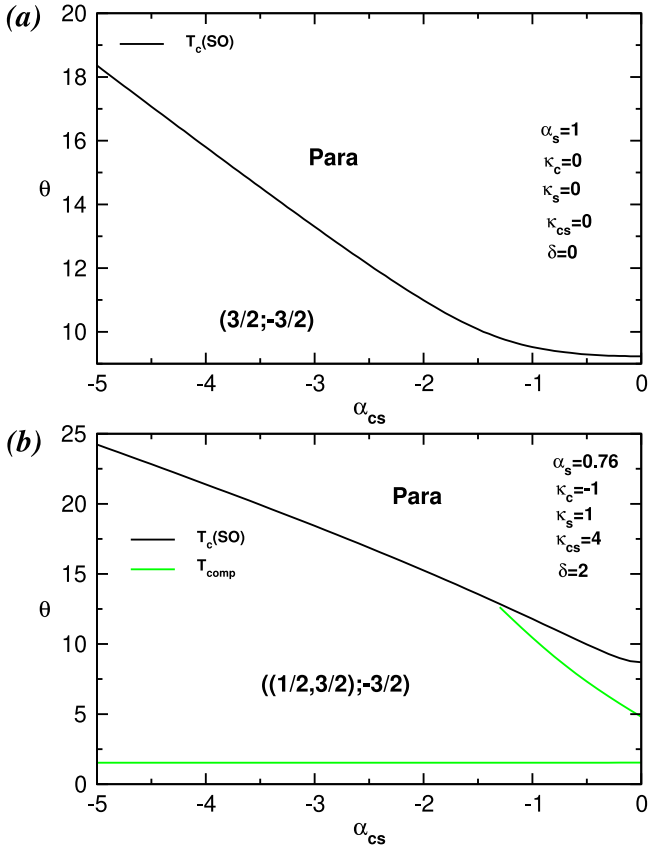

Fig. 8. The dependency of both transition and compensation temperatures on the interlayer exchange α_{cs} when (a) $\alpha_s = 1$, $\kappa = 0$, $\kappa_{cs} = 0$ and $\delta = 0$ and (b) $\alpha_s = 0.76$, $\kappa_s = 1$, $\kappa_c = -1$, $\kappa_{cs} = 4$ and $\delta = 2$.

$$\forall j \in \{c_1, c_2, \ldots, c_6; s_1, s_2, s_3\}.$$

Finally, the core magnetization m_c, the shell magnetization m_s and the total magnetization m_t are calculated as follows

$$m_c = \frac{m_{c1} + 6m_{c2} + 6m_{c3} + 6m_{c4} + 6m_{c5} + 12m_{c6}}{37}, \tag{7}$$

$$m_s = \frac{6m_{s1} + 12m_{s2} + 6m_{s3}}{24}, \tag{8}$$

$$m_t = \frac{37m_c + 24m_s}{61}. \tag{9}$$

In the next section, we numerically solve the main equations presented above to study the thermal and external magnetic field changes of magnetizations for given values of J_μ, K_μ and Δ_μ and thus to obtain the phase diagrams on possible planes of our parameter space.

3. Numerical findings and discussion

3.1. Ground states phase diagrams

In this subsection, the ground states (GS) phase diagrams of the hexagonal Ising nanowire with core–shell structure are mapped when the external magnetic field is set to zero. The Hamiltonian given in Eq. (1) is used to calculate the energy of possible configurations of the model at $T = 0.0$. Then the allowed GS is determined by picking the configuration with lowest possible energy. Since the model is symmetric, one can restrict the shell with negative spin values and the core with positive spin values when the external magnetic field is zero. Also, to simplify the system, a uniform distribution of spin values on the sublattices of shell, a uniform distribution of spin values on the outer sublattices i.e. (c_5, c_6) of the core

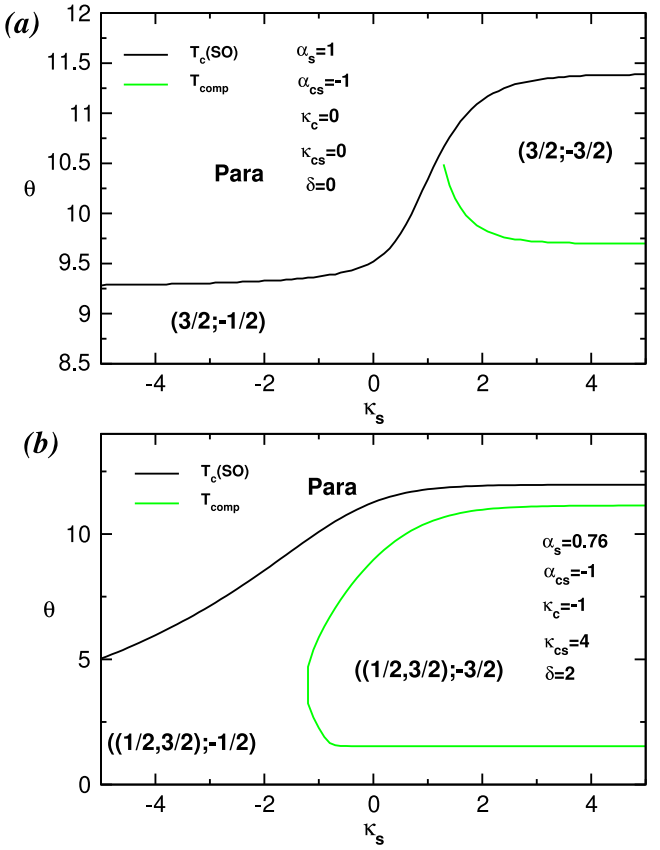

Fig. 9. The dependency of both transition and compensation temperatures on the intralayer exchange κ_s when (a) $\alpha_s = 1$, $\kappa_c = 0$, $\kappa_{cs} = 0$ and $\delta = 0$ and (b) $\alpha_s = 0.76$, $\alpha_{cs} = -1$, $\kappa_c = -1$, $\kappa_{cs} = 4$ and $\delta = 2$.

and a uniform distribution of spin values on the inner sublattices i.e. (c_1, c_2, c_3, c_4) of the core are assumed. This allows us to set

$$S^{s1} = S^{s2} = S^{s3}, \tag{10}$$

$$S^{c5} = S^{c6}, \tag{11}$$

$$S^{c1} = S^{c2} = S^{c3} = S^{c4}. \tag{12}$$

where S^{s1}, S^{s2}, S^{s3} are the common spin values on the sublattices of the shell for example. This makes $2 \times 2 \times 2 = 8$ possible configurations of the system. The configurations are noted in the form (a, b) where a denotes the spin value on the core and b denotes the spin value on the shell or in the form $((a, b), c)$ where a denotes the spin value on the core interior and b denotes the spin value on the core exterior and c denotes the spin value on the shell. In addition, the reduced quantities $\theta = k_B T/J$, $\alpha_s = J_s/J$, $\alpha_{cs} = J_{cs}/J$, $\kappa_c = K_c/J$, $\kappa_s = K_s/J$, $\kappa_{cs} = K_{cs}/J$, $\delta_c = \Delta_c/J$, $\delta_s = \Delta_s/J$ and $H = h/J$ are used to simplify the notation.

In Fig. 3, the GS phase diagrams are obtained on the (α_s, δ_s) plane when $\alpha_{cs} = -1$ and $\delta_c = 0$ (Fig. 3*a*), on the (α_s, δ_c) plane for $\alpha_{cs} = -1$ and $\delta_s = 5$ (Fig. 3*b*) and on the (α_s, δ) plane by setting $\alpha_{cs} = -1$ and $\delta = \delta_c = \delta_s$ (Fig. 3*c*) when the biquadratic interactions are turned off, i.e. $\kappa = \kappa_c = \kappa_s = 0$ and $\kappa_{cs} = 0$. As shown in Fig. 3*a*, we observe two stable states namely $(\frac{3}{2}, -\frac{3}{2})$ and $(\frac{3}{2}, -\frac{1}{2})$ separated by an ascending line with respect to α_s. It is clear that increasing α_s values strengthen the shell spins in the configuration $-\frac{3}{2}$. On the other hand, when δ_s exceeds a given threshold limit, the shell spins take the value $-\frac{1}{2}$. In Fig. 3*b*, we distinguish four stable states obtained by the competition between α_s and δ_c. One observes, $(\frac{3}{2}, -\frac{1}{2})$ for low α_s and δ_c, $(\frac{1}{2}, -\frac{3}{2})$ for high α_s and δ_c, $(\frac{1}{2}, -\frac{1}{2})$ for low α_s and high δ_c, and $(\frac{3}{2}, -\frac{3}{2})$ for high α_s and low δ_c. They are all separated by straight lines, except $(\frac{1}{2}, -\frac{1}{2})$ and $(\frac{3}{2}, -\frac{3}{2})$ configurations which are bordered by an ascending line according to α_s. In Fig. 3*c*, we also find the four stable states as in Fig. 3*b* but now the two straight α_s-lines become ascending.

To examine the effects of interlayer coupling α_{cs}, the GS phase diagrams are obtained again for $\kappa = \kappa_c = \kappa_s = 0$ and $\kappa_{cs} = 0$ as illustrated in Fig. 4. Fig. 4*a* shows it on the (α_{cs}, δ_s) plane when $\alpha_s = 1$ and $\delta_c = 0$. One observes two

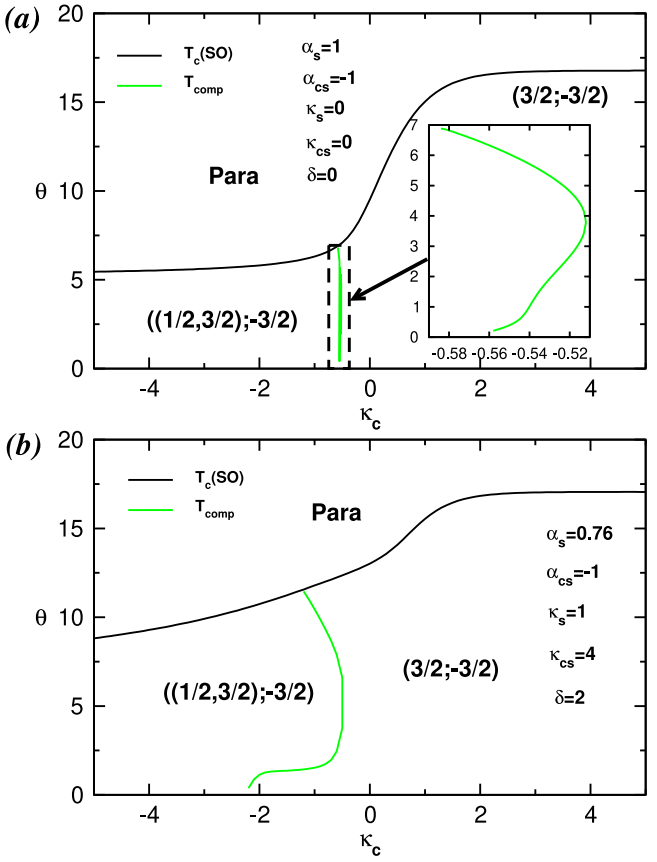

Fig. 10. The dependency of both transition and compensation temperature on the intralayer exchange κ_c when (*a*) $\alpha_s = 1$, $\kappa_s = 0$, $\kappa_{cs} = 0$ and $\delta = 0$ and (*b*) $\alpha_s = 0.76$, $\alpha_{cs} = -1$, $\kappa_s = 1$, $\kappa_{cs} = 4$ and $\delta = 2$.

stable states $(\frac{3}{2}, -\frac{3}{2})$ and $(\frac{1}{2}, -\frac{3}{2})$ separated by a descending line in regard to α_{cs}. The core spins flip from $\frac{3}{2}$ to $\frac{1}{2}$ when δ_c exceeds a given limit value. Fig. 4*b* is calculated on the (α_{cs}, δ_c) plane when $\alpha_s = 1$ and $\delta_s = 0$. Now four stable states $(\frac{3}{2}, -\frac{3}{2})$, $(\frac{1}{2}, -\frac{3}{2})$, $((\frac{3}{2}, \frac{1}{2}), -\frac{3}{2})$ and $((\frac{1}{2}, \frac{3}{2}), -\frac{3}{2})$ are observed. It appears thus two new states constituted in the core, of a mixed spins $\frac{3}{2}$ and $\frac{1}{2}$. The (α_{cs}, δ) GS phase diagram is obtained when $\alpha_s = 1$ with $\delta = \delta_c = \delta_s$ as shown in Fig. 4*c*. Now, we distinguish five stable states namely $(\frac{3}{2}, -\frac{3}{2})$, $(\frac{3}{2}, -\frac{1}{2})$, $(\frac{1}{2}, -\frac{1}{2})$, $((\frac{3}{2}, \frac{1}{2}), -\frac{3}{2})$ and $((\frac{3}{2}, \frac{1}{2}), -\frac{1}{2})$.

In Fig. 5, the effects of both δ_s and δ_c are displayed on the GS phase diagrams of the system. They are mapped on the (δ_c, δ_s) plane for selected values of interlayer coupling α_{cs} when $\alpha_s = 1$ and $\kappa = 0$ and $\kappa_{cs} = 0$. It is found that when $|\alpha_{cs}|$ is lower, for example $|\alpha_{cs}| = 0.1$ as demonstrated in Fig. 5*a*, six stable states are observed namely $(\frac{3}{2}, -\frac{3}{2})$, $(\frac{3}{2}, -\frac{1}{2})$, $(\frac{1}{2}, -\frac{3}{2})$, $(\frac{1}{2}, -\frac{3}{2})$, $((\frac{3}{2}, \frac{1}{2}), -\frac{3}{2})$ and $((\frac{3}{2}, \frac{1}{2}), -\frac{1}{2})$. For $|\alpha_{cs}| = 1$ (Fig. 5*b*), the mixed states in the core disappear and we observe four stable states which are $(\frac{3}{2}, -\frac{3}{2})$, $(\frac{3}{2}, -\frac{1}{2})$, $(\frac{1}{2}, -\frac{3}{2})$ and $(\frac{1}{2}, -\frac{3}{2})$. But when $|\alpha_{cs}|$ is higher, i.e. $|\alpha_{cs}| = 1.5$ (Fig. 5*c*), the state $((\frac{1}{2}, \frac{3}{2}), -\frac{1}{2})$ appears in addition to the four states of Fig. 5*b*.

The last GS phase diagrams including the effects of κ are delineated in Fig. 6. Fig. 6*a* represents it on the (κ_c, δ) plane when $\alpha_s = 1$, $\alpha_{cs} = -1$, $\kappa_s = 0$ and $\kappa_{cs} = 0$ in which five stable states of the system $(\frac{3}{2}, -\frac{3}{2})$, $(\frac{3}{2}, -\frac{1}{2})$, $(\frac{1}{2}, -\frac{3}{2})$, $(\frac{1}{2}, -\frac{1}{2})$ and $((\frac{1}{2}, \frac{3}{2}), -\frac{3}{2})$ are found. Six GS states are captured as $(\frac{3}{2}, -\frac{3}{2})$, $(\frac{3}{2}, -\frac{1}{2})$, $(\frac{1}{2}, -\frac{1}{2})$, $((\frac{1}{2}, \frac{3}{2}), -\frac{3}{2})$, $((\frac{3}{2}, \frac{1}{2}), -\frac{3}{2})$ and $((\frac{3}{2}, \frac{1}{2}), -\frac{1}{2})$ on the (κ_{cs}, δ) plane when $\alpha_s = 1$, $\alpha_{cs} = -1$ and $\kappa = 1$ indicated in Fig. 6*b*. The (κ, δ) plane GS phase diagram is for $\alpha_s = 1$, $\alpha_{cs} = -1$ and $\kappa_{cs} = 0$ (Fig. 6*c*). It shows four states given as $(\frac{3}{2}, -\frac{3}{2})$, $(\frac{3}{2}, -\frac{1}{2})$, $(\frac{1}{2}, -\frac{1}{2})$ and $((\frac{1}{2}, \frac{3}{2}), -\frac{3}{2})$. The final one, i.e. Fig. 6*d*, is obtained on the (κ, δ) plane with $\alpha_s = 1$, $\alpha_{cs} = -1$ and $\kappa_{cs} = -1$. Three new states appear namely $(\frac{3}{2}, -\frac{1}{2})$, $((\frac{1}{2}, \frac{3}{2}), -\frac{3}{2})$, $((\frac{3}{2}, \frac{1}{2}), -\frac{1}{2})$ in addition to the states obtained when $\kappa_{cs} = 0$ (Fig. 6*c*).

We note that the competition between different interaction parameters enriches the GS phase diagrams of the system. Thus, the GS states of the model is diversified by the given spin values when more parameters are turned on. Nevertheless, the system remains dominated by the $(\frac{3}{2}, -\frac{3}{2})$ state. After having obtained the GS phase diagrams at zero T, we are now ready to obtain the T-dependent phase diagrams with the help of GS phase diagrams in the next section.

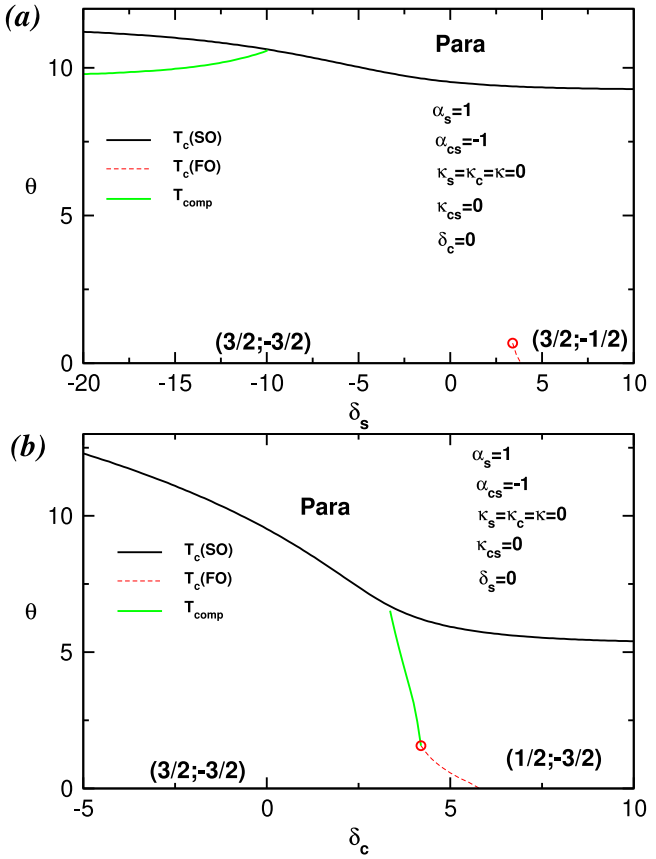

Fig. 11. The dependency of both transition and compensation temperatures on the crystal field δ_s (a) when $\alpha_s = 1$, $\kappa = 0$, $\kappa_{cs} = 0$ and $\delta_c = 0$ and on the crystal field δ_c (b) when $\alpha_s = 0$, $\alpha_{cs} = -1$, $\kappa = 0$, $\kappa_{cs} = 0$ and $\delta_s = 0$.

3.2. Phases diagrams at zero magnetic field

In this work we use mean field theory to investigate the magnetic properties of an Ising nanowire spin-$\frac{3}{2}$ with a hexagonal core–shell structure. The numerical results are obtained by solving Eqs. (5) and (6) iteratively. The solid black, red dashed, and solid green lines in the phase diagrams denoted the second-order, first-order, and compensation lines, respectively. In addition, the full black circle, the full black square and the empty red circle represent respectively the tricritical point, the critical end-point and the isolated critical point.

In Fig. 7, we plot the dependencies of both transition and compensation temperatures on intralayer exchange α_s when $\alpha_{cs} = -1$, $\kappa = 0$, $\kappa_{cs} = 0$ and $\delta = 0$ (Fig. 7a), as well as $\alpha_{cs} = -1$, $\kappa_s = 1$, $\kappa_c = -1$, $\kappa_{cs} = 4$ and $\delta = 2$ (Fig. 7b). The phase diagram in Fig. 7a clearly shows only a second-order phase transition line from the ordered phase $(\frac{3}{2}, -\frac{3}{2})$ to the paramagnetic phase. The phase transition temperature increases with α_s. Furthermore, when α_s is greater than 1.82, the model exhibits a compensation line that decreases progressively as α_s increases and appears to have an asymptotic limit when α_s is large enough. As in the previous figure, the model in Fig. 7b depicts a second-order phase transition line that increases with increasing α_s. Two compensation temperatures are also observed. Indeed, the system exhibits a double compensation behavior for $0.304 \leq \alpha_s \leq 0.81$. One obtained at constant temperature $\theta = 1.53$ and the second one obtained at high temperature increases with α_s. However, when $\alpha_s > 0.81$, the model exhibits a single compensation behavior at constant temperature $\theta = 1.53$.

In Fig. 8, we display the dependencies of both transition and compensation temperatures on the interlayer exchange α_{cs} when $\alpha_s = 1$, $\kappa = 0$, $\kappa_{cs} = 0$ and $\delta = 0$ (Fig. 8a) and when $\alpha_s = 0.76$, $\kappa_s = 1$, $\kappa_c = -1$ and $\kappa_{cs} = 4$ (Fig. 8b). Fig. 8a demonstrates that the transition from the ordered phase to the paramagnetic phase is of second order and that the transition temperature increases with $|\alpha_{cs}|$. To better understand the influence of the coupling α_{cs} on the compensation temperatures of the system, we set $\alpha_s = 0.76$ and kept the other parameters at the values shown in Fig. 7b. As a result, we get Fig. 8b, which shows two compensation temperature lines: one that stays constant at $\theta = 1.53$ for all α_{cs} and the other that increases with α_{cs} and disappears when $\alpha_{cs} > 1.3$.

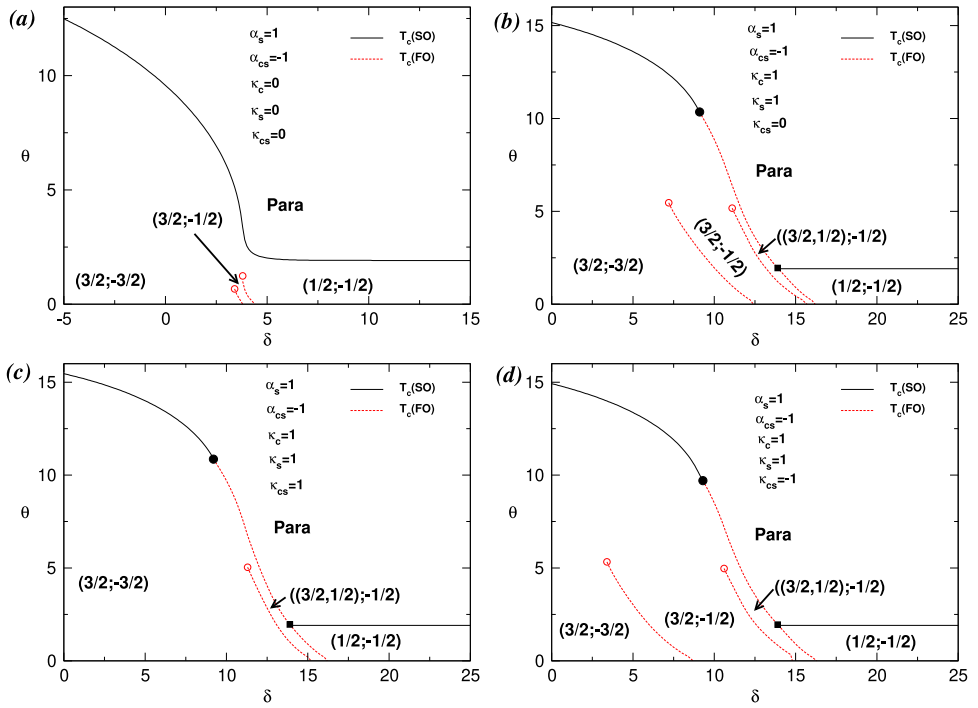

Fig. 12. The dependency of both transition and compensation temperature on the crystal field δ for (a) when $\alpha_s = 1$, $\kappa = 0$ and $\kappa_{cs} = 0$, (b) when $\alpha_s = 1$, $\alpha_{cs} = -1$, $\kappa = 1$ and $\kappa_{cs} = 0$, (c) when $\alpha_s = 1$, $\alpha_{cs} = -1$, $\kappa = 1$ and $\kappa_{cs} = 1$ and (d) when $\alpha_s = 1$, $\alpha_{cs} = -1$, $\kappa = 1$ and $\kappa_{cs} = -1$.

Fig. 9 depicts the effects of intralayer exchange κ_s on transition and compensation temperatures when $\alpha_s = 1, \alpha_{cs} = -1$, and $\kappa_c = 0$, $\kappa_{cs} = 0$ and $\delta = 0$ (Fig. 9*a*) and when $\alpha_s = 0.76$, $\alpha_{cs} = -1$ $\kappa_c = -1$ and $\kappa_{cs} = 4$ (Fig. 9*b*). Fig. 9*a* shows two ordered phases of the system: $(\frac{3}{2}, -\frac{3}{2})$ and $(\frac{3}{2}, -\frac{1}{2})$. When $\kappa_s \leq 0$ the system is in the $(\frac{3}{2}, -\frac{1}{2})$ phase, but when $\kappa_s > 0$ the system is in the $(\frac{3}{2}, -\frac{3}{2})$ phase. The transition from the ordered to the paramagnetic phase is continuous, and the critical temperatures rise with increasing κ_s before falling to asymptotic constant values as $\kappa_s \rightarrow \pm\infty$. For $\kappa_s > 1.3$, the model has one compensation temperature that decreases progressively as κ_s increases and reaches an asymptotic value $\theta = 9.7$. As shown in Fig. 9*b*, the system illustrates two ordered phases, $((\frac{1}{2}, \frac{3}{2}), -\frac{1}{2})$ and $((\frac{1}{2}, \frac{3}{2}), -\frac{3}{2})$, when $\kappa_s \leq 0$ and $\kappa_s > 0$, respectively. Double compensation behavior is observed when $\kappa_s \geq -1.2$. In fact, two compensation lines with asymptotic values of $\theta = 1.53$ and $\theta = 11.14$ for the lower and upper sections at higher κ_s begin to decline as κ_s declines and they turn back to each other and meet at roughly $\kappa_s = -1.2$.

The intralayer exchange κ_c dependence of the transition and compensation temperatures when $\alpha_s = 1$, $\alpha_{cs} = -1$, $\kappa_s = 0$, $\kappa_{cs} = 0$ and $\delta = 0$ and when $\alpha_s = 0.76$, $\alpha_{cs} = -1$ $\kappa_s = 1$, $\kappa_{cs} = 4$ and $\delta = 2$ are displayed in Fig. 10*a-b*, respectively. In the first, we identify two ordered phases of the system as functions of κ_c namely $((\frac{1}{2}, \frac{3}{2}), -\frac{3}{2})$ and $(\frac{3}{2}, -\frac{3}{2})$. The second-order phase line increases as a function of κ_c. The model's compensatory behaviors are seen at the boundary of the two ordered phases. In fact, one obtains single compensation behavior for $-0.584 \leq \kappa_c \leq -0.558$ while observing double compensation behavior for $-0.558 \leq \kappa_c \leq -0.512$. Given the selected parameter values, one can observe in Fig. 10*b* that the compensation behaviors are nearly identical to those in Fig. 10*a*, but now the range of compensation temperatures has expanded, i.e., $-2.2 \leq \kappa_c \leq -1.1$.

As seen in Fig. 11, when $\alpha_s = 1$, $\alpha_{cs} = -1$, and all other parameters are set to zero, we have constructed the phase diagrams in the (δ_s, θ) and (δ_c, θ) planes. Again of second order, the phase transition line lowers with increasing δ_s and δ_c. As a function of δ_s, we obtain two ordered phases, $(\frac{3}{2}, -\frac{3}{2})$ and $(\frac{3}{2}, -\frac{1}{2})$, which are separated by a first-order transition line that begins at $(\delta_s = 3.85, \theta = 0)$ and terminates at the isolated critical point $(\delta_s = 3.4, \theta = 0.68)$. Similarly, as a function of δ_c (Fig. 11*b*), we likewise obtain two ordered phases, $(\frac{3}{2}, -\frac{3}{2})$ and $(\frac{1}{2}, -\frac{3}{2})$, which are separated by a first-order transition line starting at $\delta_s = 5.8, \theta = 0$ and ending at the isolated critical point at $\delta_c = 4.2, \theta = 1.57$. One magnetic compensation behavior is observed for $\delta_s \leq -10$, and for $3.36 \leq \delta_c \leq 4.2$, the model also produces one magnetic compensation line that terminates at the end of the first-order phase transition line.

Fig. 12 allows us to understand the influence of the uniform crystal field δ on the phase diagram of the system when $\alpha_s = 1$, $\alpha_{cs} = -1$ for selected values of κ and κ_{cs}. For $\kappa = 0$ and $\kappa_{cs} = 0$ (Fig. 12*a*), one observes a continuous phase transition line which separates the ordered phase from the paramagnetic phase, decreases as δ increases and then stabilizes for large δ. When $\kappa = 1$, tricritical behavior is seen in Fig. 12*b-d* produced for $\kappa_{cs} = 0, 1, -1$, respectively.

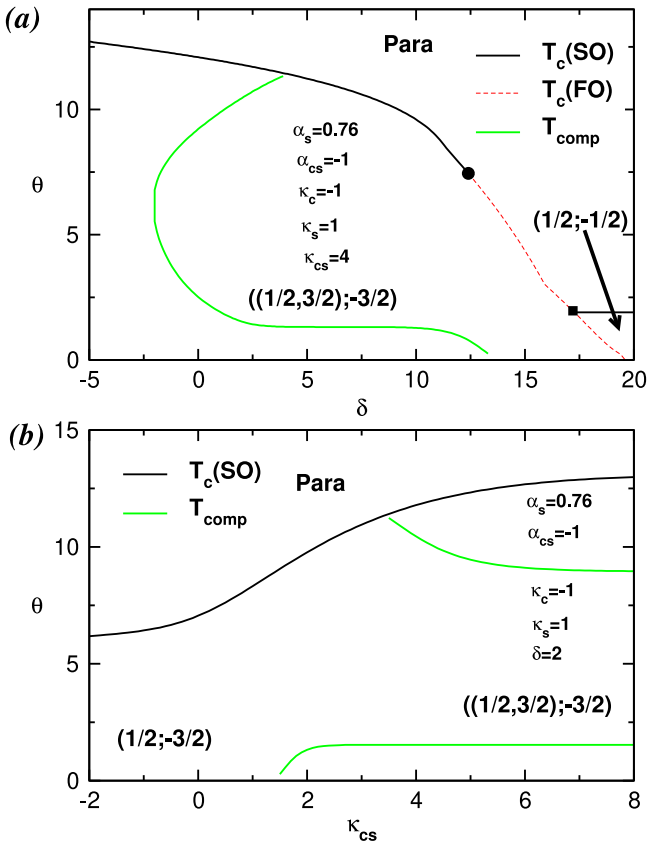

Fig. 13. The dependency of both transition and compensation temperatures for (a) on the crystal field δ when $\alpha_s = 0.76$, $\alpha_{cs} = -1$, $\kappa_s = 1$, $\kappa_c = -1$ and $\kappa_{cs} = 4$ and (b) on the interlayer exchange κ_{cs} when $\alpha_s = 0.76$, $\alpha_{cs} = -1$, $\kappa_s = 1$, $\kappa_c = -1$ and $\delta = 2$.

Note that the tricritical point is the intersection of the first- and second-order phase transition lines. For $\kappa = 0$ and $\kappa_{cs} = 0$ (Fig. 12a) we identify three ordered phases of the system separated by two first-order phase transition lines. The first one, which separates phases $(\frac{3}{2}, -\frac{3}{2})$ and $(\frac{3}{2}, -\frac{1}{2})$, begins at $(\delta = 3.8, \theta = 0)$ and finishes at the isolated critical point $(\delta = 3.4, \theta = 0.66)$. The second one starting at $(\delta = 4.4, \theta = 0)$ and ending at the isolated critical point $(\delta = 3.8, \theta = 0.99)$ separates the phases $(\frac{3}{2}, -\frac{1}{2})$ and $(\frac{1}{2}, -\frac{1}{2})$. In addition to the other two phases from Fig. 12a, a new first-order phase transition line between the phases $(\frac{3}{2}, -\frac{1}{2})$ and $((\frac{3}{2}, \frac{1}{2}), -\frac{1}{2})$ can be seen in Fig. 12b. The first-order phase transition line separating the phases $(\frac{3}{2}, -\frac{3}{2})$ and $(\frac{3}{2}, -\frac{1}{2})$ disappears in the Fig. 12c. The phase diagram in Fig. 12d is similar to that of Fig. 12b, but now the first-order phase transition lines between two ordered phases separated further from each other. The straight portion of the second-order lines as seen in the last three phase diagrams separate the ordered phase $(\frac{1}{2}, -\frac{1}{2})$ from the paramagnetic phase at large values of δ and terminate on the first-order lines at the critical end points.

Fig. 13 is obtained for $\alpha_s = 0.76$, $\alpha_{cs} = -1$ and $\kappa_s = 1$ shows the dependency of transition and compensation temperatures on the uniform crystal field δ when $\kappa_c = -1$ and $\kappa_{cs} = 4$ (Fig. 13a) and on the interlayer exchange κ_{cs} when $\delta = 2$ (Fig. 13b). The first one demonstrates that the critical lines resemble those in Fig. 12b. When $\delta < 17.2$, the model is in the ordered phase $((\frac{1}{2}, \frac{3}{2}), -\frac{3}{2})$. Two compensation lines are observed for $-2.5 < \delta < 3.9$, but for $3.9 < \delta < 13.3$ it reduces to one. Again the critical end-point is observed which separates the ordered phase $(\frac{1}{2}, -\frac{1}{2})$ from the paramagnetic phase for large δ. As illustrated in Fig. 13b, only a second-order phase transition line resembling the one in Fig. 10b is discovered. One of the compensation line starts near the critical line around of $(\kappa_{cs} = 3.5, \theta = 11.238)$, decreases progressively with increasing κ_{cs} and stabilizes for large values of κ_{cs}, while the second one also starts around of $(\kappa_{cs} = 1.52, \theta = 0.283)$, increases very slowly before stabilizing around a constant value of the temperature for large values of κ_{cs}.

The phase diagrams that are displayed in this section demonstrate that the system exhibits a wide range of unique and fascinating magnetic properties. Our found results are in good agreement with those reported in Refs. [42,50–52].

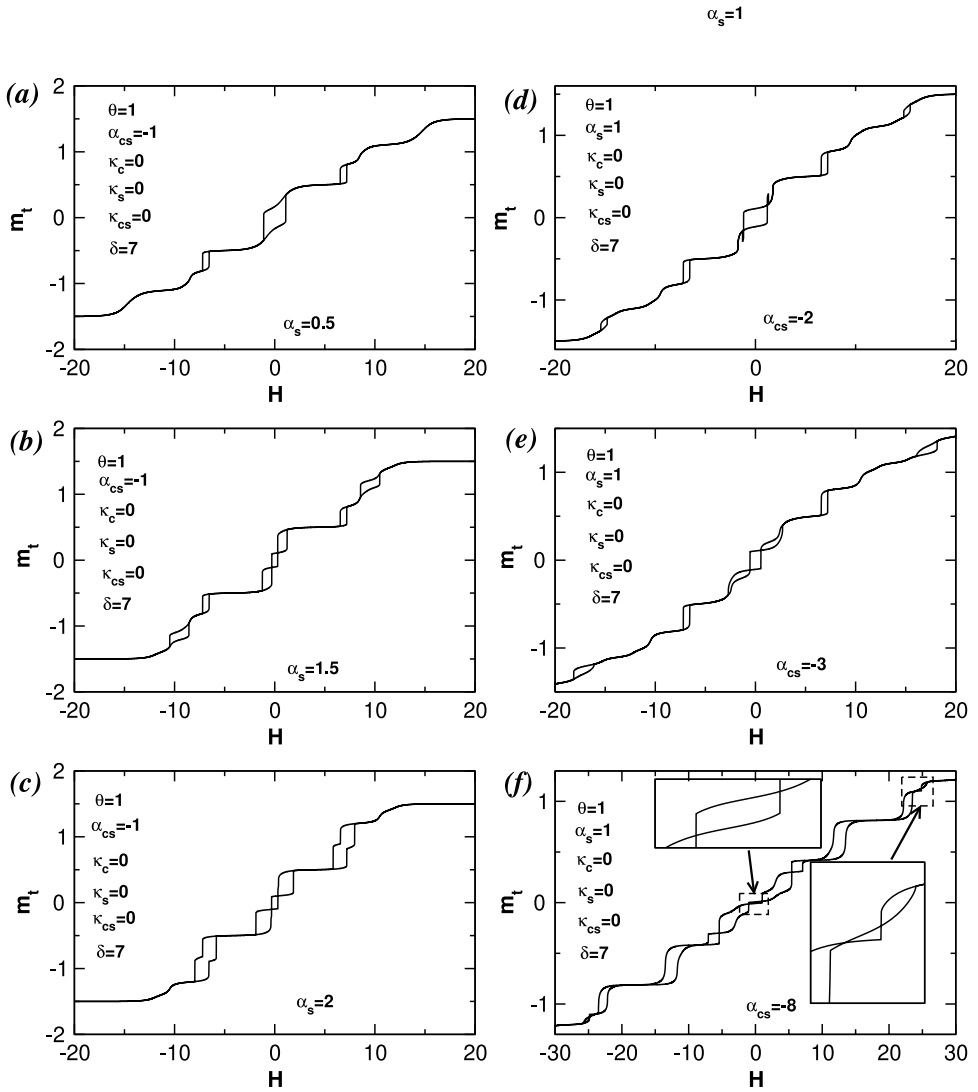

Fig. 14. The hysteresis loops of m_t for $(a\text{-}c)$ for various values of the intralayer exchange α_s when $\theta = 1$, $\alpha_{cs} = -1$, $\kappa = 0$, $\kappa_{cs} = 0$ and $\delta = 7$ and $(d\text{-}f)$ for various values of the interlayer exchange α_{cs} when $\theta = 1$, $\alpha_s = 1$, $\kappa = 0$, $\kappa_{cs} = 0$ and $\delta = 7$.

3.3. Hysteresis loops

In order to highlight the influence of the system parameters on the magnetic hysteresis cycles behavior, we have plotted the total magnetization curves of the system as a function of the external magnetic field H.

The hysteresis cycles in Fig. 14 are obtained for $\theta = 1$, $\kappa = 0$, $\kappa_{cs} = 0$ and $\delta = 7$ with given values of intralayer exchange $\alpha_s = 0.5, 1.0, 1.5$ when $\alpha_{cs} = -1$ (Fig. 14*a-c*) and that of interlayer exchange given as $\alpha_{cs} = -2, -3, -8$ with $\alpha_s = 1$ (Fig. 14*d-f*), respectively. In these hysteresis cycles, the total magnetization evolves gradually as a function of the magnetic field H with several horizontal panels. When $\alpha_s = 0.5$, we see three magnetic hysteresis cycles, one at the center and two on each side. Two more magnetic hysteresis cycles develop at the sides and the central cycle triples, creating a total of seven hysteresis cycles when α_s rises to 1.5. Increasing α_s further to 2, the two hysteresis cycles at each side merge together reducing the total number of the cycles to five. For $\alpha_{cs} = -2, -3$ (Fig. 14*d-e*) we get five magnetic hysteresis cycles with a central one whose width decreases with $|\alpha_{cs}|$. But for $\alpha_{cs} = -8$ (Fig. 14*f*) the number of hysteresis cycles increases considerably to thirteen hysteresis cycles including a central one.

Fig. 15 shows the magnetic hysteresis loops for $\theta = 1$, $\alpha_s = 1$, $\alpha_{cs} = -1$, $\kappa_{cs} = 0$ and $\delta = 0$. Fig. 15*a-c* illustrates them for various values of intralayer exchange $\kappa_s = -0.5, -1.0, -4.0$ when $\kappa_c = 0$ and Fig. 15*d-f* is for various values of $\kappa_c = -0.1, -0.2, -1.0$ when $\kappa_s = 0$. According to the different panels of these figures, we observe that

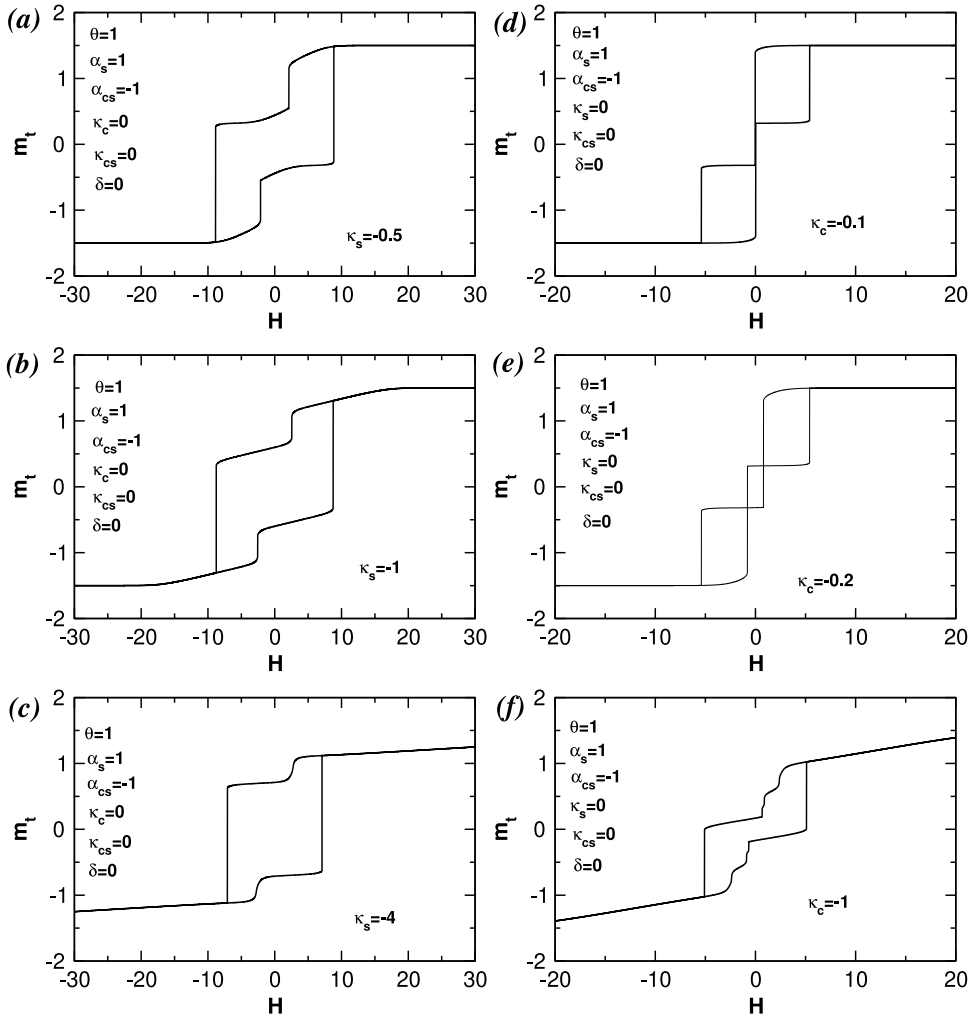

Fig. 15. The hysteresis loops of m_t when $(a\text{-}c)$ for various values of the intralayer exchange κ_s when $\theta = 1$, $\alpha_s = 1$, $\alpha_{cs} = -1$, $\kappa_c = 0$, $\kappa_{cs} = 0$ and $\delta = 0$ and $(d\text{-}f)$ for various values of the intralayer exchange κ_c when $\theta = 1$, $\alpha_s = 1$, $\alpha_{cs} = -1$, $\kappa = 0$, $\kappa_{cs} = 0$ and $\delta = 0$.

magnetic hysteresis cycles whose width progressively decreases when κ_s becomes more and more negative. The number of hysteresis cycles changes as a function of κ_c: two cycles when $\kappa_c = -0.1$, three cycles when $\kappa_c = -0.2$ and one hysteresis cycle when $\kappa_c = -1$.

Fig. 16 expresses the magnetic hysteresis loops when $\theta = 1, \kappa = 0.5, \alpha_s = 1$ and $\alpha_{cs} = -1$. In addition, Fig. 16*a-c* shows the first three for $\delta = 0$ and $\kappa_{cs} = -1, -1.5, -2$ and Fig. 16*d-f* displays the last three for $\delta = 3$ and $\kappa_{cs} = -0.5, -1.7, -2$. The number of hysteresis cycles starts with one for $\kappa_{cs} = -1$, increases to five for $\kappa_{cs} = -1.5$ and increases again to seven when $\kappa_{cs} = -2$ for Fig. 16*a-c*. And, the number of hysteresis cycles again starts with one when $\kappa_{cs} = -0.5$, increases to nine when $\kappa_{cs} = -1.7$ and decreases to five when $\kappa_{cs} = -2.5$ for Fig. 16*d-f*.

Fig. 17 illustrates the magnetic hysteresis loops for $\theta = 1$, $\kappa_c = -0.5$, $\kappa_s = 0$, $\alpha_s = 1$, $\alpha_{cs} = -1$ and $\kappa_{cs} = 0$. Fig. 17*a-c* is obtained by keeping $\delta_c = 7$ constant for given $\delta_s = 6, 7, 8$ and Fig. 17*d-f* is plotted for fixed $\delta_s = 5$ for given $\delta_c = 5, 10, 15$. When δ_s increases the width of magnetic hysteresis cycles increases. For $\delta_s = 6$ and $\delta_s = 7$ nine magnetic hysteresis cycles are found but for $\delta_s = 8$ thirteen of them are found. For $\delta_c = 5$, a single hysteresis cycle made of several horizontal portions are observed. For $\delta_c = 10, 15$ some parts overlap giving nine magnetic hysteresis cycles.

To illustrate the effects of temperature on magnetic hysteresis loops, they are plotted by increasing temperatures $\theta = 0.5, 1.5, 8, 9.3, 10$ and 13.47 as demonstrated in Fig. 18. We notice that the number of magnetic hysteresis cycles of the system can vary according to the temperature of the system. Above the critical temperature from the ordered phase to the paramagnetic phase, the magnetic hysteresis cycles disappear as expected.

The model parameters greatly influence the magnetic behaviors of the system as a function of the external magnetic field by strengthening or weakening the cooperativity between the sites of the system. Several magnetic hysteresis

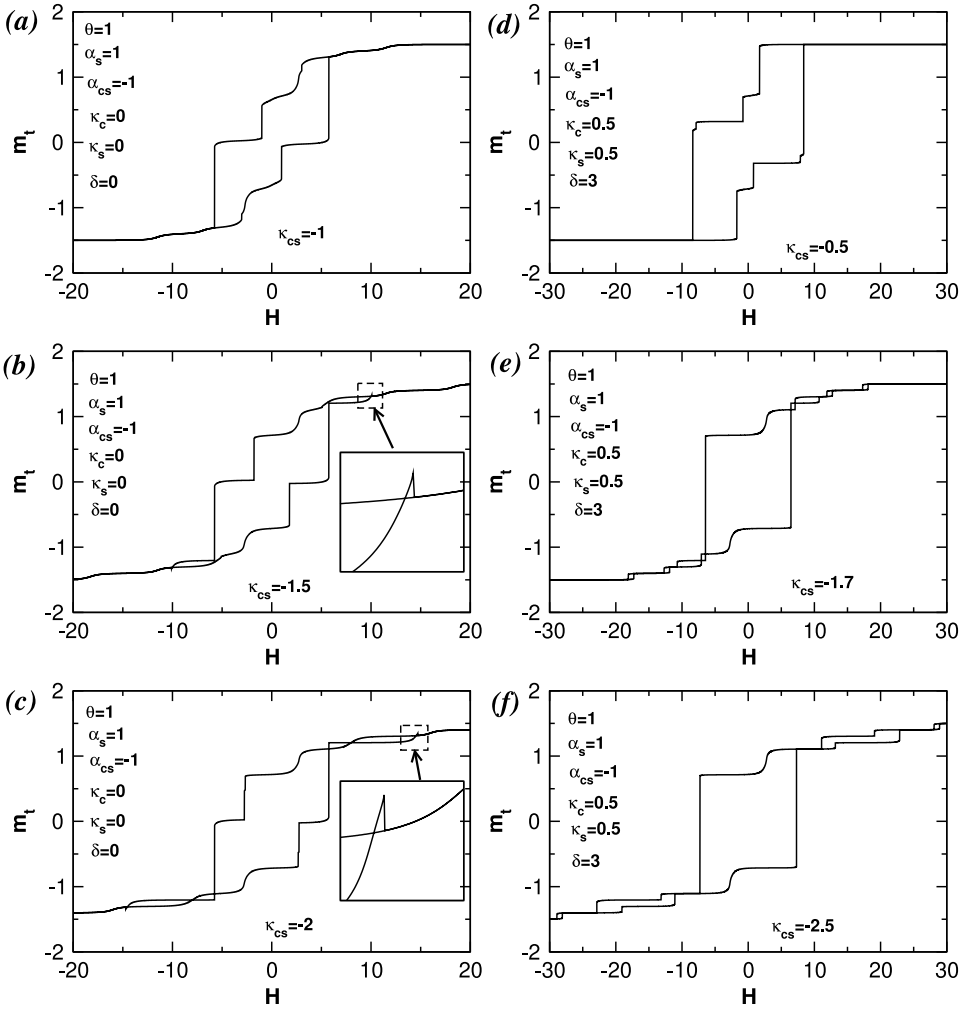

Fig. 16. The hysteresis loops of m_t when $(a\text{-}c)$ for various values of the interlayer exchange κ_{cs} when $\theta = 1$, $\alpha_s = 1$, $\alpha_{cs} = -1$, $\kappa = 0$, and $\delta = 0$ and $(d\text{-}f)$ for various values of the interlayer exchange κ_{cs} when $\theta = 1$, $\alpha_s = 1$, $\alpha_{cs} = -1$, $\kappa = 0.5$, and $\delta = 3$.

behaviors can be revealed by making judicious choices of the system parameters values. The different panels reflect the local or asymptotic stability of the system under the constraint of the external magnetic field. The magnetic hysteresis cycles illustrate the multiplicity of the system state for certain chosen values of the external magnetic field. These magnetic properties have many technological applications. Some magnetic hysteresis loops reported in this section look similar to those found in Refs. [52–54].

4. Conclusion

In this work, we have used the mean field approximation based on the Gibbs–Bogoliubov inequality for the free energy to investigate the magnetic features of a hexagonal Ising nanowire spin-$\frac{3}{2}$ with a core–shell structure. First, we have plotted ground state phase diagrams in different planes of system parameters. Then, we have investigated system parameters' effects on the phase diagrams and on the hysteresis behaviors when applying the external magnetic field. The obtained results show that the model presents first-order and second-order phase transitions lines, in addition to tricritical points, critical end-points and isolated critical points. In specific range of values of the model exchange interaction parameters, the model yields the possibility of single or double compensation behaviors. It is also noted that double compensation appear when the system core is in a mixed phase state. Finally, we have noted the existence of multiple hysteresis loops behavior depending on the model parameters. Our found results are in good agreement with those obtained in other works in literature.

We believe that our theoretical investigation could stimulate further research on the critical properties of nanostructure systems and also motivate experimenters to investigate their compensation and multiple hysteresis behaviors.

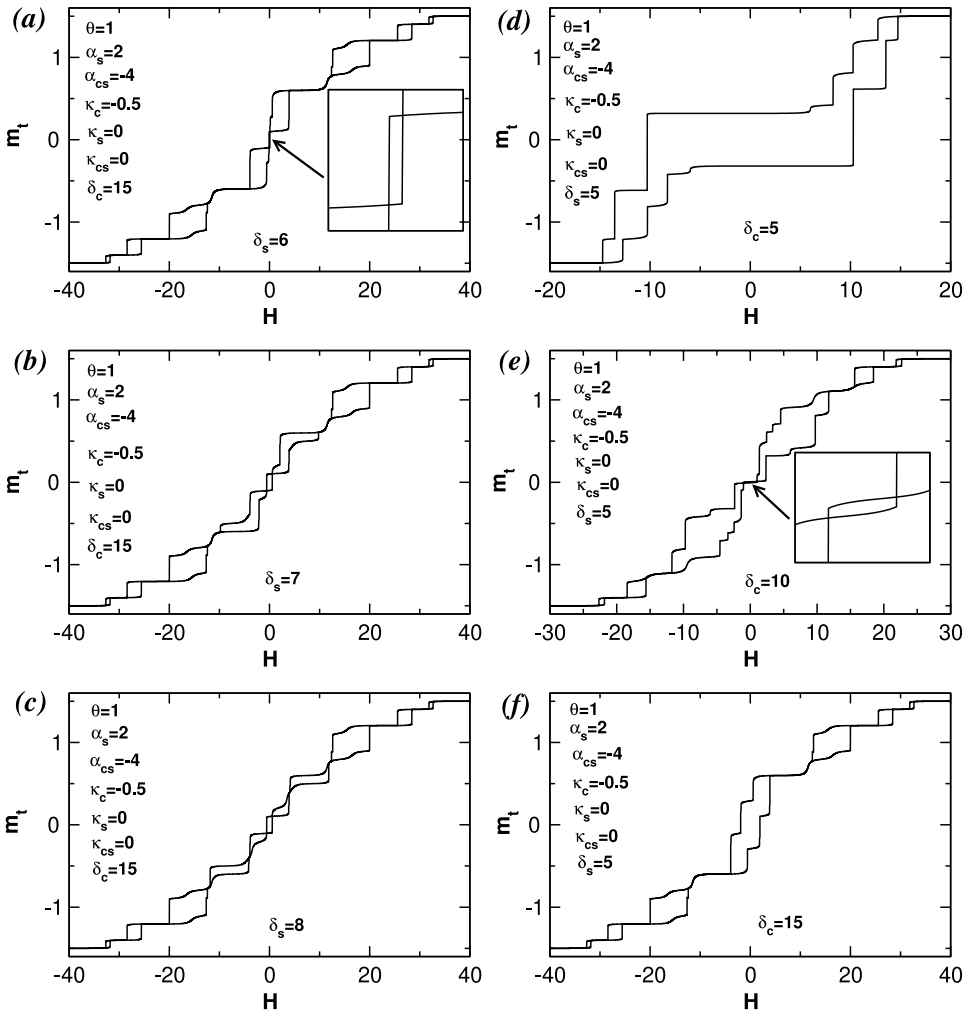

Fig. 17. The hysteresis loops of m_t when (a-c) for different values of the crystal field δ_s when $\theta = 1$, $\alpha_s = 2$, $\alpha_{cs} = -4$, $\kappa_s = 0$, $\kappa_c = -0.5$, $\kappa_{cs} = 0$ and $\delta - c = 15$ and (d-f) for different values of the crystal field δ_c when $\theta = 1$, $\alpha_s = 2$, $\alpha_{cs} = -4$, $\kappa_s = 0$, $\kappa_c = -0.5$, $\kappa_{cs} = 0$ and $\delta_s = 5$.

CRediT authorship contribution statement

G.B. Aziza Goguin: Carried out all the calculations. **T.D. Oke:** Given advise for carrying out all the calculations. **R.A.A. Yessoufou:** Supervision, Methodology, Writing – review & editing. **E. Albayrak:** Supervision, Methodology, Writing – review & editing.

Declaration of competing interest

The authors declare that they have no known competing financial interests or personal relationships that could have appeared to influence the work reported in this paper.

Data availability

No data was used for the research described in the article.

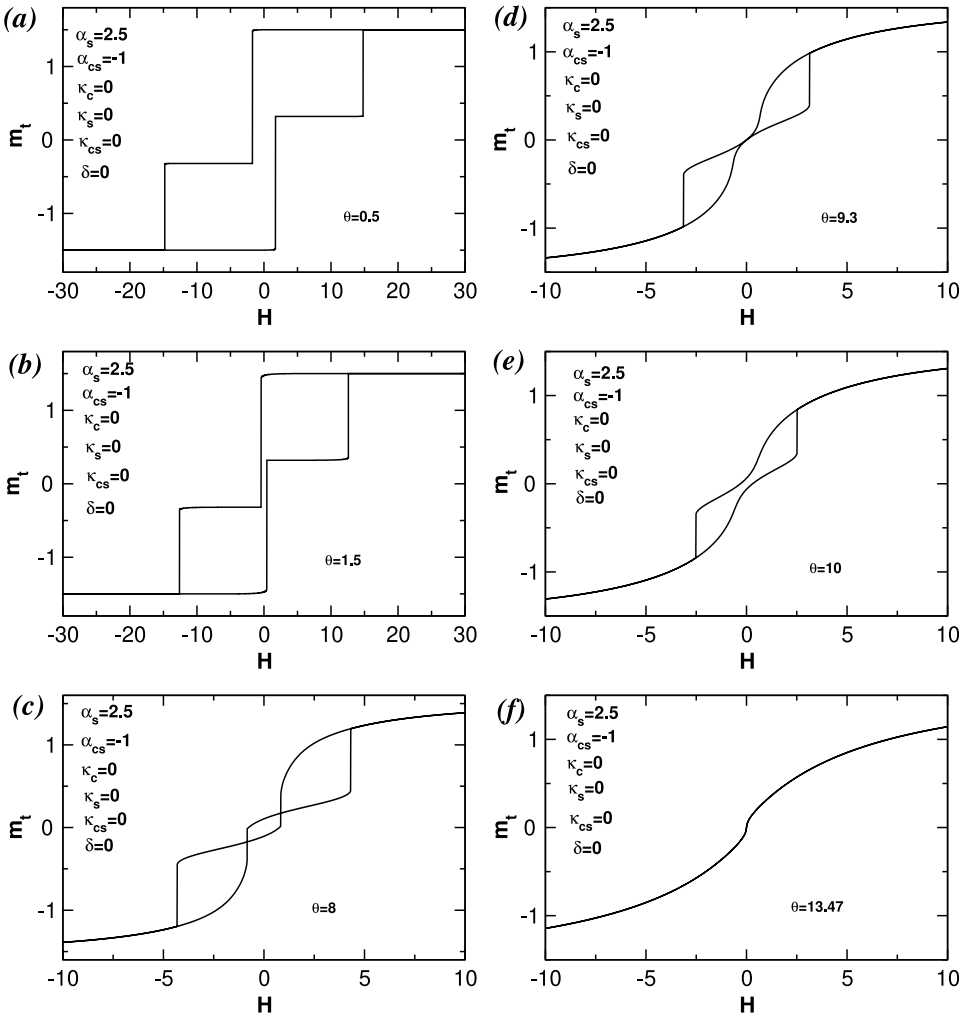

Fig. 18. The hysteresis loops of m_t for various values of the temperature when $\theta = 1$, $\alpha_s = 2.5$, $\alpha_{cs} = -1$, $\kappa = 0$, $\kappa_{cs} = 0$ and $\delta = 0$.

References

[1] C.L. Chien, G.C. Hadjipanayis, G.A. Prinz, Science and Technology of Nanostructured Magnetic Materials, Plenum Press, New York, 1991, p. 4772.
[2] R. Skomsk, J. Phys. Condens. Matter 15 (2003) R841.
[3] C. Zhu, M. Wang, T.J. Li, T. Lu, L.K. Pan, Ionics 23 (2017) 2175.
[4] A.M. Saleem, V. Desmaris, P. Enoksson, J. Nanomater. (2016) 1537269.
[5] T. Maurer, F. Ott, G. Chaboussant, Y. Soumare, J.Y. Piquemal, G. Viau, Appl. Phys. Lett. 91 (2007) 172501.
[6] S.L. Viñas, R. Salikhov, C. Bran, E.M. Palmero, M. Vazquez, B. Arvan, X. Yao, P. Toson, J. Fidler, M. Spasova, U. Wiedwald, M. Farle, Nanotechnology 26 (2015) 415704.
[7] J.F. Scott, Annu. Rev. Mater. Sci. 28 (1998) 79.
[8] A.I. Kingon, S.K. Streiffer, C. Basceri, C.R. Summerfelt, MRS Bull. 21 (1996) 46.
[9] Y. Ye, B. Geng, Crit. Rev. Solid State Mater. Sci. 37 (2012) 75.
[10] S.J. Son, J. Reichel, B. He, M. Schuchman, S.B. Lee, J. Am. Chem. Soc. 127 (2005) 7316.
[11] C.A. Haberzettl, Nanotechnology 13 (2002) R9.
[12] S. Khizroev, M.H. Kryder, D. Litvinov, D.A. Thompson, Appl. Phys. Lett. 81 (2002) 2256.
[13] R. Vajtai, Springer Handbook of Nanomaterials. Book, 2013.
[14] Y.S. Hwang, S.H. Park, J.W. Lee, Polymers 9 (2017) 13.
[15] R. Yendluri, D.P. Otto, M.M. De Villiers, V. Vinokurov, Y.M. Lvov, Int. J. Pharm. 521 (2017) 267.
[16] A.L. Hemasa, N. Naumovski, W.A. Maher, A. Ghanem, Nanomaterials 7 (2017) 186.
[17] R.G. Chaudhuri, S. Paria, Chem. Rev. 112 (2012) 2373.
[18] X.Y. Kong, Y. Ding, Z.L. Wang, J. Phys. Chem. B 108 (2004) 570.
[19] Z. Dong, L.H. Cai, F.S. Wen, F.S. Li, Chinese J. Chem. Phys. 20 (2007) 821.
[20] J.F. Ye, H.J. Zhang, R. Yang, X.G. Li, L.M. Qi, Small 6 (2010) 296.

[21] T. Kaneyoshi, J. Magn. Magn. Mater. 322 (2010) 3014.
[22] M. Ertaş, E. Kantar, Phase Transit. 88 (2015) 567.
[23] T. Kaneyoshi, J. Magn. Magn. Mater. 322 (2010) 3410.
[24] T. Kaneyoshi, J. Magn. Magn. Mater. 323 (2011) 2483.
[25] T. Kaneyoshi, Phys. Status Solidi b 248 (2011) 250.
[26] T. Kaneyoshi, Physica A 391 (2012) 3616.
[27] T. Kaneyoshi, Physica A 392 (2013) 2406.
[28] T. Kaneyoshi, J. Magn. Magn. Mater. 420 (2016) 303.
[29] Y. Kocakaplan, E. Kantar, M. Keskin, Eur. Phys. J. B 86 (2013) 420.
[30] Y. Kocakaplan, E. Kantar, Chin. Phys. B 23 (2014) 046801.
[31] B. Boughazi, M. Boughrara, M. Kerouad, J. Magn. Magn. Mater. 354 (2014) 173.
[32] M. Boughrara, M. Kerouad, A. Zaim, J. Magn. Magn. Mater. 360 (2014) 222.
[33] Y. Yüksel, Phys. Rev. E 91 (2015) 032149.
[34] T. Kaneyoshi, J. Supercond. Nov. Magn. 30 (2017) 1867.
[35] T. Kaneyoshi, Physica A 390 (2011) 3697.
[36] T. Kaneyoshi, Solid State Commun. 151 (2011) 1528.
[37] O. Canko, A. Erdinç, F. Taşkın, A.F. Yıldırım, J. Magn. Magn. Mater. 324 (2012) 508.
[38] W. Wang, Y. Liu, Z.-Y. Gao, X.-R. Zhao, Y. Yang, S. Yang, Physica E 101 (2018) 110.
[39] V.G. Kostishyn, A.T. Morchenko, D.N. Chitanov, J. Alloys Compd. 586 (2014) S317.
[40] B. Boughazi, M. Boughrara, M. and Kerouad, Physica A 465 (2017) 628.
[41] H. Falk, Amer. J. Phys. 38 (1970) 858.
[42] N. Hachem, I.A. Badrour, A. El Antari, A. Lafhal, M. Madani, M. El Bouziani, Chinese J. Phys. 71 (2021) 12.
[43] Z. Fadil, N. Saber, H. Eraki, A. Mhirech, B. Kabouchi, L. Bahmad, Spin 12 (2022) 2250020.
[44] Y. Kocakaplan, M. Ertaş, J. Exp. Theor. Phys. 121 (2015) 606.
[45] E. Kantar, M. Keskin, J. Supercond. Nov. Magn. 29 (2016) 2387.
[46] E. Kantar, M. Ertaş, J. Supercond. Nov. Magn. 28 (2015) 2529.
[47] Z. Elmaddahi, M. El Hafidi, M.Y. El Hafidi, Physica E 122 (2020) 114123.
[48] Y. Kocakaplan, M. Keskin, J. Appl. Phys. 116 (2014) 093904.
[49] M. Blume, V.J. Emery, R.B. Griffiths, Phys. Rev. A 4 (1971) 1071.
[50] Z. Elmaddahi, M. Marsi, M. Hafidi, J. Magn. Magn. Mater. 564 (2022) 170046.
[51] A. Kadiri, G.D. Ngantso, M. Ait Tamerd, R. Kumar, M. Arejdal, A. Abbassi, Y. El Amraoui, H. Ez-Zahraouy, A. Benyoussef, Solid State Commun. 352 (2022) 114816.
[52] Brahim Boughazi, O. Amhoud, M. Kerouad, J. Supercond. Nov. Magn. 35 (2022) 1123.
[53] B. Nmaila, K. Htoutou, R. Ahllaamara, L.B. Drissi, Indian J. Phys. 97 (2023) 429.
[54] N. Hachem, Y. Al Qahoom, R. Aharrouch, M. Madani, M. El Bouziani, Romanian J. Phys. 67 (2022) 9.